

Early-type Galaxies on the Star Formation Main Sequence: Internal Star Formation Geometry Revealed with MaNGA and Their Environmental Origin

SHUHEI KOYAMA,¹ YUSEI KOYAMA,^{1,2} TAKUJI YAMASHITA,¹ MASAHIRO KONISHI,³ KOSUKE KUSHIBIKI,¹ AND KENTARO MOTOHARA^{3,1}

¹*National Astronomical Observatory of Japan, 2-21-1 Osawa, Mitaka, Tokyo 181-8588, Japan*

²*Department of Astronomical Science, Graduate University for Advanced Studies (SOKENDAI), 2-21-1 Osawa, Mitaka, Tokyo 181-8588, Japan*

³*Institute of Astronomy, Graduate School of Science, The University of Tokyo, 2-21-1 Osawa, Mitaka, Tokyo 181-0015, Japan*

ABSTRACT

Star-forming galaxies on the main sequence (MS) are often regarded as a uniform population characterized by similar global star formation properties. However, there exists a diversity in galaxy morphologies at fixed stellar mass and SFR. In this study, using spatially-resolved properties from the MaNGA final data release, we classify MS galaxies into late-type (MS-late) and early-type (MS-early). In addition, we further divide the MS-early galaxies into two distinct subgroups based on their internal star formation and stellar mass distributions within the galaxies. The first group—“MS-early_SF”—shows centrally concentrated star formation without prominent stellar bulges and resides preferentially in dense environments, suggesting environmentally-driven evolution. The second group—“MS-early_stellar”—exhibits significant stellar bulges with suppressed central star formation, maintains disk-like star formation patterns, and inhabits environments similar to those of late-type galaxies, indicating evolution through internal secular processes. Our findings demonstrate that spatially-resolved observations play critical roles in revealing the diverse evolutionary pathways hidden within galaxies that share similar global properties.

Keywords: galaxies: evolution — galaxies: ISM — galaxies: star formation

1. INTRODUCTION

Galaxy evolution is influenced by a combination of many processes, including star formation, galaxy morphology, active galactic nuclei (AGN), environmental effects, and more. Understanding how these processes are related is essential for revealing the mechanisms behind galaxy evolution. Over the last few decades, large-scale surveys have provided extensive data, allowing for detailed studies of galaxy properties and their relations. One of the most well-established relationships in galaxy evolution is the star formation main sequence (MS), a tight correlation between the stellar mass (M_*) and star formation rate (SFR) of star-forming galaxies across various environments (Daddi et al. 2007; Elbaz et al. 2007; Peng et al. 2010; Koyama et al. 2013). Galaxies on the MS are considered to be undergoing steady-state star formation, while those above and below the

relation are classified as starbursts and passive galaxies, respectively. Morphology is another key aspect of galaxy evolution, and it is closely related to star formation activity. The majority of star-forming galaxies on the MS have late-type morphologies, suggesting that typical star-forming galaxies are characterized by disk structures and steady, mass-dependent star formation activity. In contrast, passive galaxies are associated with early-type morphologies. This observed connection between star formation activity and morphology suggests an evolutionary sequence where star-forming galaxies located on the MS eventually evolve into passive galaxies through the quenching of their star formation and accompanying morphological transformation (Wuyts et al. 2011; Bell et al. 2012).

Large integral field spectroscopy (IFS) surveys such as MaNGA (Bundy et al. 2015) and SAMI (Croom et al. 2012) provide spatially-resolved spectroscopic data for thousands of nearby galaxies, enabling statistical studies of internal star formation properties. These surveys

have revealed important insights by examining galaxies based on their position relative to the MS or their morphological types. For example, studies have found that star-forming galaxies on the MS tend to have relatively flat sSFR profiles, indicating steady-state star formation throughout their disks. In addition, central suppression of sSFR has been observed in high-mass star-forming galaxies, interpreted as a signature of inside-out quenching (e.g., Belfiore et al. 2018; Ellison et al. 2018).

While previous studies have provided important insights by examining galaxies based on their MS position or morphological types, there is evidence that star-forming galaxies on the MS are not a uniform population. Galaxy morphology catalogs based on large-scale optical imaging surveys, such as Galaxy Zoo 1 and 2 (Lintott et al. 2011; Willett et al. 2013), have shown a variety in galaxy morphologies among MS galaxies, including a non-negligible fraction of early-type galaxies in addition to the dominant late-type population. This morphological variety is one clear example of the diversity within the MS population. Medling et al. (2018) studied resolved star formation properties of galaxies with different morphologies and reported that some early-type galaxies are found in the MS. While those early-type galaxies on the MS show average sSFR profiles similar to those of late-type galaxies, they also reported significant scatter in resolved properties among individual galaxies. This scatter suggests that global properties like MS position or morphology may not fully represent the diversity of MS galaxies, and that examining internal galaxy structure and star formation distributions can reveal different populations within the MS.

Additional processes such as AGN feedback and environmental effects are particularly important to consider, as they can significantly influence both galaxy structure and star formation activity. AGN can affect the distribution and properties of star-forming gas through feedback processes (Fabian 2012; Harrison 2017), while environmental mechanisms like galaxy interactions and ram pressure stripping can reshape both the morphology and star formation activity of galaxies (Boselli & Gavazzi 2006; Blumenthal & Barnes 2018). Understanding how these processes relate to the observed diversity in star formation distributions may provide crucial insights into the different evolutionary pathways of MS galaxies.

In this paper, we investigate the diversity of MS galaxies using the final data release of the MaNGA survey. After classifying MS galaxies based on their morphology, we first quantify their spatially-resolved star formation and stellar mass distributions through Sérsic profile fitting. Based on these structural properties, we then analyze the radial profiles of specific star formation

rates and resolved main sequence relations to characterize their star formation patterns in detail. Finally, we examine how these characteristics correlate with AGN activity and environment to understand the origin of the observed diversity. Through this analysis, we aim to reveal evolutionary pathways hidden within the MS diversity.

This paper is organized as follows. Section 2 describes the MaNGA survey data, our sample selection criteria, and the derived properties used in our analysis. Section 3 presents our main results, including the Sérsic profile fitting of Σ_{SFR} and Σ_* maps, the comparison of mean sSFR radial profiles, and the resolved main sequence relations. The discussion is presented in Section 4, where we explore how AGN and environment relate to the observed diversity of star formation distributions, and discuss possible evolutionary pathways. Finally, we summarize our findings in Section 5. Throughout this paper, we adopt a Λ CDM cosmology with $H_0 = 67.7$ km s⁻¹ Mpc⁻¹ and $\Omega_M = 0.310$ (Planck 2018: Planck Collaboration et al. 2020), and the Kroupa (2001) initial mass function (IMF).

2. DATA

2.1. The MaNGA Survey

MaNGA (Bundy et al. 2015) is one of the three core programs of the 4th generation of the Sloan Digital Sky Survey (SDSS-IV; Blanton et al. 2017). The survey uses the 2.5m Sloan Foundation Telescope at the Apache Point Observatory (Gunn et al. 2006) and employs 17 different sized integral field unit (IFU) fiber bundles, ranging from 19 to 127 fibers with a diameter of 2 arcsec. The spectra cover a wavelength range of 3600–10300 Å at a spectral resolution of $R \sim 2000$. The target galaxies are selected from the NASA-Sloan Atlas catalog with a redshift range of $0.01 < z < 0.15$, and is designed to be representative of the overall galaxy population at $z \sim 0.03$ and covers a wide range of galaxy properties, including stellar mass, color, and morphology. The MaNGA observing strategy employs dithered observations to ensure uniform spatial sampling across each galaxy. The final data cubes have a spatial resolution of $\sim 2.5''$ (FWHM), which corresponds to a typical physical resolution of 1.5 kpc at the median redshift of the survey ($z \sim 0.03$).

2.2. Sample Selection

The sample is drawn from the final data release of the MaNGA survey, the Data Release 17 (DR17; Abdurro'uf et al. 2022), and the Marvin software (Cherinka et al. 2019) is employed to access and analyze the data. The MaNGA data is processed through two main pipelines:

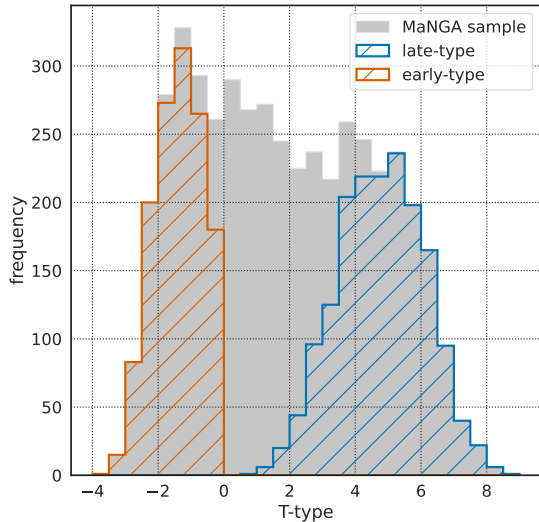


Figure 1. The histogram of T-type from the MaNGA Morphology Deep Learning DR17 catalog for the full sample (gray) and the samples classified as late-type (blue) and early-type (red) galaxies based on the T-type and P_LTG values.

the Data Reduction Pipeline (DRP; Law et al. 2016) and the Data Analysis Pipeline (DAP; Westfall et al. 2019). The DRP provides sky-subtracted and flux-calibrated 3D spectra for each galaxy. The DAP provides two-dimensional maps of measured properties obtained through stellar continuum fitting and emission line measurements on the spectra produced by the DRP. In this study, we use the VOR10-MILESHC-MASTARS maps included in the DAP, in which a spatial binning is performed by the Voronoi binning algorithm (Cappellari & Copin 2003) to achieve a signal-to-noise ratio (S/N) ~ 10 in the g-band per spectral pixel for each bin (Aguado et al. 2019).

The sample selection is based on the DAPall catalog, which is a summary table of the DAP. The selection criteria require that the maps are generated correctly as indicated by the DAPDONE flag being True, and that the data is free from quality issues (DAPQUAL=0). The sample is limited to galaxies with $z < 0.05$, corresponding to a spatial resolution of 2.5 kpc at the typical seeing of $2.5''$. Additionally, we apply NSA_ELLPETRO_BA > 0.5 to select galaxies with an elliptical petrosian B/A ratio greater than 0.5. The sample consists of 4706 galaxies.

We perform morphological classification using the MaNGA Morphology Deep Learning DR17 catalog (Domínguez Sánchez et al. 2022), which provides deep learning-based morphological classifications trained on two visually-based morphological catalogs (Nair & Abraham 2010; Willett et al. 2013). The T-type is a

numerical classification scheme that ranges from -4 to 9, with positive values indicating spiral galaxies of increasingly later types. The P_LTG parameter represents the probability of a galaxy being late-type, with values ranging from 0 (early-type) to 1 (late-type). In this paper, we combine these parameters with conservative thresholds, to select galaxies with distinct morphologies (i.e. early-type and late-type). We define "early-type" galaxies as those with T-type ≤ 0 and P_LTG < 0.1 , and "late-type" galaxies as those with T-type > 0 and P_LTG > 0.9 . This classification yields 1697 late-type and 1330 early-type galaxies. Since visually-based morphological classifications can be affected by spatial resolution and color variations (e.g., Masters et al. 2021; Ren et al. 2024; Salvador et al. 2024; Foster et al. 2025), we verify the reliability of our morphological classification by examining the correlation between T-type and Sérsic index from NSA r-band measurements, finding a strong anti-correlation (correlation coefficient $r = -0.7$) as expected. The Sérsic index is more robust against poor spatial resolution and agnostic to color. We calculate residuals from the T-type vs Sérsic index relation and confirm that these residuals show only weak correlations with redshift, SDSS g-r color, or spatial resolution (FWHM/Re) (correlation coefficients $r = 0.05, 0.007$, and -0.2 , respectively), indicating that systematic effects from distance, color, or spatial resolution have minimal impact on our morphological classifications within our sample. In Figure 1, we show the histogram of the T-type for the full sample (in gray histogram) and the samples classified as late-type and early-type galaxies (in red and blue shaded histograms, respectively).

2.3. Derived properties

The emission line measurements are taken from the emline_gflux maps in the MaNGA DAP. These maps are derived through a two-step process in the DAP pipeline (Westfall et al. 2019). First, the stellar continuum is modeled and subtracted from each spectrum using a combination of stellar templates from the MILES stellar library (Sánchez-Blázquez et al. 2006). This step accounts for stellar absorption features that could affect emission line measurements, particularly for Balmer lines. After the continuum subtraction, the emission lines are fit using Gaussian profiles. Using these emission line measurements, we derive the star formation rate surface density (Σ_{SFR}) from the H α and H β emission line maps. First, we calculate the Balmer decrement (H α /H β ratio) to estimate dust attenuation at each spaxel, assuming Case B recombination and the Cardelli et al. (1989) attenuation curve. The dust-corrected H α

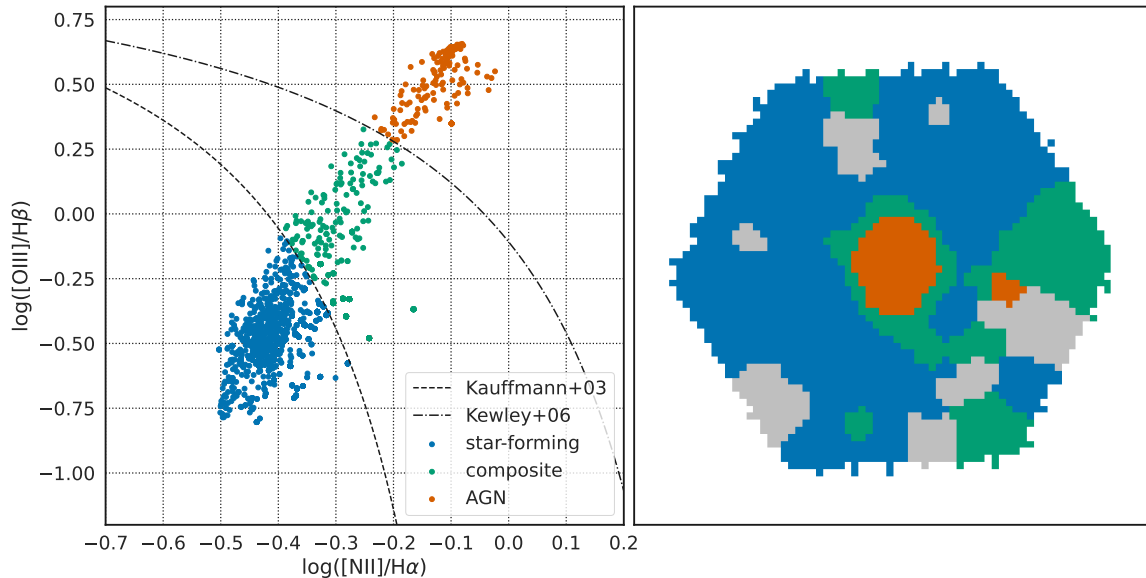


Figure 2. An example of the resolved BPT diagram. The left panel shows the $[\text{N II}]/\text{H}\alpha$ vs. $[\text{O III}]/\text{H}\beta$ line ratios for individual spaxels, with the demarcation lines from Kauffmann et al. (2003) (dashed line) and Kewley et al. (2006) (dash-dotted line). Spaxels are classified as star-forming (blue), composite (green), or AGN (red) based on their locations relative to these lines. The right panel displays the spatial distribution of the classified spaxels within the galaxy using the same color scheme. Spaxels with $S/N < 3$ in $\text{H}\alpha$, $\text{H}\beta$, $[\text{N II}]$, or $[\text{O III}]$ are shown in grey.

luminosity is then converted to Σ_{SFR} using the calibration from Kennicutt et al. (1994).

We also construct the resolved BPT (Baldwin et al. 1981) diagram to distinguish star-forming regions from other ionization sources on a spaxel-by-spaxel basis using $\text{H}\alpha$, $\text{H}\beta$, $[\text{N II}]$, and $[\text{O III}]$ maps. In Figure 2, we show an example of the resolved BPT diagram. Based on Kauffmann et al. (2003) and Kewley et al. (2006), we distinguish star-forming, composite and AGN spaxels. Throughout this paper, we exclude spaxels classified as AGN or composite from our analysis of star formation properties (Σ_{SFR} and SFR) to measure pure star formation activity uncontaminated by other ionization sources.

The stellar mass surface density (Σ_*) is obtained from the MaNGA Firefly Stellar Populations value-added catalog (Goddard et al. 2017; Neumann et al. 2022). This catalog provides spatially resolved stellar population properties derived using the FIREFLY spectral fitting code (Wilkinson et al. 2017), which performs a full spectral fitting to the stellar continuum using the MaStar stellar population models (Maraston et al. 2020).

Finally, we calculate the total star formation rate (SFR) by summing up the Σ_{SFR} of the spaxels classified as star-forming for each galaxy. The total stellar mass (M_*) is derived by summing up the Σ_* from all spaxels. To validate our measurement methods, we compare our measurements with those from the GALEX-SDSS-WISE Legacy Catalog 2 (GSWLC-2; Salim et al. 2016, 2018),

which derives M_* and SFR through UV/optical/mid-IR SED fitting. The measurements show tight correlation with scatter of 0.2 dex for both SFR and M_* . We find that our SFR measurements are typically 0.1 dex higher and our M_* measurements are 0.2 dex lower than the GSWLC-2 values. This offset in SFR may be related to several methodological factors, including the different timescales measured by $\text{H}\alpha$ versus UV+IR techniques (Kennicutt & Evans 2012), spatially-resolved dust corrections, and differences in calibration assumptions. While we cannot determine the contribution of each factor, the overall offset is relatively small compared to the scatter between the two measurements (0.2 dex). For the stellar mass, this offset is consistent with Neumann et al. (2022), who reported that Firefly-derived total stellar masses (MaStar model) are typically 0.05-0.32 dex lower than other catalog masses due to differences in stellar population models and fitting methodologies. Most importantly, since our sample selection is based on the relative position of galaxies in the M_* -SFR parameter space using our own measurements, these systematic offsets do not affect our analysis.

Furthermore, to assess potential biases in our SFR measurements from excluding AGN/composite spaxels, we perform an additional test. For MS galaxies hosting AGN/composite spaxels, we compare two measurements of total SFR. The first includes only star-forming spaxels, while the second additionally includes AGN and composite spaxels. This second measurement provides

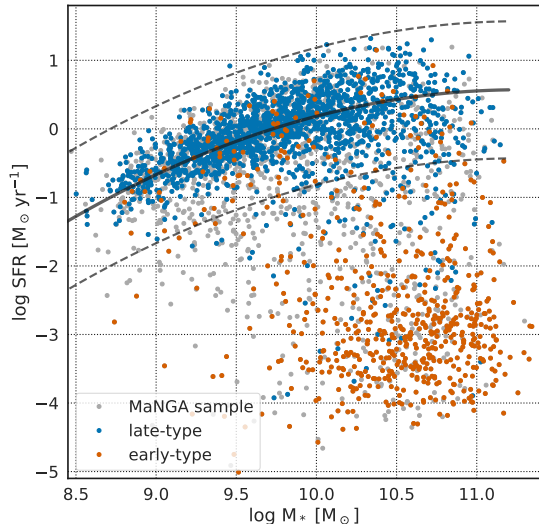


Figure 3. The relation between total stellar mass (M_*) and total star formation rate (SFR) for the morphology classified sample. Blue circles show late-type galaxies, while red circles show early-type galaxies. The black solid line indicates the best-fit star-formation main sequence relation. The dashed lines show the ± 1 dex scatter around the main sequence relation.

an upper limit on the potential star formation activity that might be obscured by AGN emission. The difference between these measurements has a median of 0.14 dex, suggesting that the exclusion of AGN/composite spaxels does not significantly affect our measurements of SFR.

2.4. MS-late and MS-early classification

In Figure 3, we show the relation between M_* and SFR for late-type and early-type galaxies. The star-formation main sequence (MS) is defined by fitting a second-order polynomial to galaxies with $\text{EW}(\text{H}\alpha) > 5$. The solid line represents the best-fitting line, while the dashed lines indicate the ± 1 dex ($\sim 3\sigma$) range. As expected, most late-type galaxies are located along the MS, while the majority of early-type galaxies are passive. However, it should be noted that a small, but non-negligible fraction of early-type galaxies are located on the MS. We classify galaxies falling within the dashed lines in Figure 3 as MS galaxies, and refer to those with late-type and early-type morphologies as the MS-late (1583 galaxies) and the MS-early (97 galaxies), respectively. Figure 4 presents examples of SDSS images of MS-late and MS-early galaxies. MS-late galaxies show typical disk-like morphology, while MS-early galaxies appear to have smooth, elliptical-like structures despite their classification as MS galaxies.

We also note that the distribution of effective radius is clearly different between MS-late and MS-early galaxies.

Figure 5 shows the relation between stellar mass and effective radius for our sample, where passive early-type galaxies are defined as early-type galaxies with SFRs below the MS as shown in Figure 3. We find that MS-late and passive early-type galaxies in our sample show a trend similar to the well-known mass-size relation (van der Wel et al. 2014), where MS-late galaxies have systematically larger sizes than passive early-type galaxies at fixed stellar mass. Interestingly, MS-early galaxies show an intermediate mass-size relation between MS-late and passive early-type galaxies, though slightly closer to the passive early-type distribution.

In the following analyses, we investigate the diversity within the MS population by comparing the MS-late and MS-early galaxies as a starting point. The main aim of this study is to study the diversity of *internal* galaxy properties among the MS galaxies, through the spatially-resolved analyses.

3. RESULTS

3.1. Sérsic Profile Analysis of Σ_{SFR} and Σ_* Maps

Our analysis aims to characterize and compare the spatial distributions of star formation activity in MS-late and MS-early galaxies. To achieve this, as a first step, we quantify the radial profiles of star formation rate surface density (Σ_{SFR}) and stellar mass surface density (Σ_*) for individual galaxies using the Sérsic profile fitting. The Sérsic profile is defined as:

$$I(r) = I_e \exp \left\{ -b_n \left[\left(\frac{r}{R_e} \right)^{1/n} - 1 \right] \right\}, \quad (1)$$

where $I(r)$ is the intensity at radius r , I_e is the intensity at the effective radius R_e , n is the Sérsic index, and b_n is a function of n that ensures half of the total luminosity is enclosed within R_e . Lower values of n indicate more uniform or late-type like distributions, while higher values represent more centrally concentrated profiles typical of bulges or elliptical galaxies. This approach allows us to simplify the complex spatial information contained in the IFS data into a set of parameters that can be easily compared across our sample, and allows us to study how star formation activity is distributed within galaxies across different morphologies.

To perform the Sérsic profile fitting, we proceed with the following steps. First, we use the elliptical coordinates of each spaxel from the galaxy center (spx_ellcoo_r_re). These coordinates account for the ellipticity and position angle of each galaxy. To account for the point spread function (PSF) effects, we convolve the Sérsic profile models with the MaNGA PSF. The PSF is well approximated by a Gaussian with a FWHM

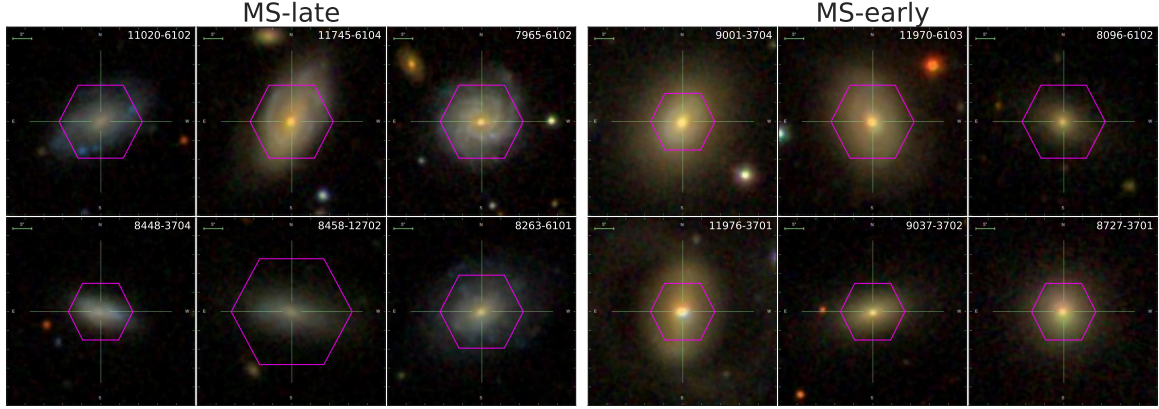


Figure 4. SDSS *gri* color composite images for six randomly selected MS-late galaxies (left panels) and MS-early galaxies (right panels). Each image is $50'' \times 50''$ in size, with the MaNGA footprint overlaid as a pink outline.

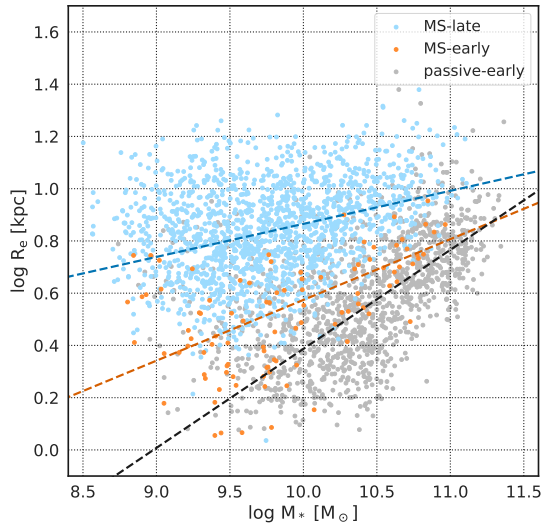


Figure 5. The relation between stellar mass and effective radius for the MS-late (blue circles), MS-early (red circles), and passive early-type (grey circles) galaxies. Lines show the best-fit linear relations for passive early-type (black dashed), MS-early (red dashed), and MS-late (blue dashed) galaxies.

of $2.54''$ (Law et al. 2016). To match the spatial binning of the observed maps, we apply the Voronoi binning scheme used in the MaNGA DAP to these PSF-convolved Sérsic maps using the BINID map. We then fit these binned, PSF-convolved Sérsic models to the observed Σ_{SFR} and Σ_* maps using a Markov Chain Monte Carlo (MCMC) approach within a Bayesian framework. This method provides probability distributions for the Sérsic indices rather than single best-fit values, allowing us to better account for uncertainties in our analysis. Figure 6 demonstrates examples of our Sérsic profile fitting for both Σ_* and Σ_{SFR} maps of the same galaxy. The radial profiles reveal different shapes with the Σ_* distribution showing a steeper decline than the Σ_{SFR} distribution. This difference is also confirmed by the

probability density distributions of the Sérsic indices, where Σ_* shows a higher Sérsic index than that of Σ_{SFR} .

Figure 7 presents the joint distribution of Sérsic indices derived from the Σ_{SFR} (n_{SFR}) and the Σ_* maps (n_*). The MS-late galaxies show a consistent pattern in their Σ_{SFR} profiles with low Sérsic indices ($n_{\text{SFR}} < 1$), indicating extended star formation activity across their disks. Their Σ_* profiles exhibit a broader distribution peaked around $n_* \sim 2$, suggesting that while all the MS-late galaxies share similar extended star formation patterns, they show more variation in their stellar mass concentration. This variation likely reflects differences in the relative prominence of central bulge components.

In contrast, the MS-early galaxies show a diversity in their structural properties. While some MS-early galaxies show concentrated stellar mass distribution (high n_*) with extended star formation (low n_{SFR}), others exhibit the opposite trend with more concentrated star formation activity despite relatively lower stellar mass concentration. For further analysis of these structural variations, we classify MS-early galaxies into two subgroups. Using the line where n_* and n_{SFR} are equal as a reference (broken line in Figure 7), we define the MS-early galaxies with $n_* > n_{\text{SFR}}$ as the “MS-early_stellar”, and those with $n_* < n_{\text{SFR}}$ as the “MS-early_SF”. Among the total 97 MS-early galaxies in our sample, 63 galaxies are classified as MS-early_SF and 34 galaxies as MS-early_stellar.

We note that some MS-early galaxies are distributed around $n_{\text{SFR}} \sim 6$, because of the limitation of our fitting procedure and the image quality of the data. This situation happens when the central star formation is more compact than the PSF size, particularly when the PSF-convolved Sérsic profile approaches the PSF shape. While it is difficult to constrain the exact values of their Sérsic indices in this case, this does not affect our main conclusion. We regard these galaxies in-

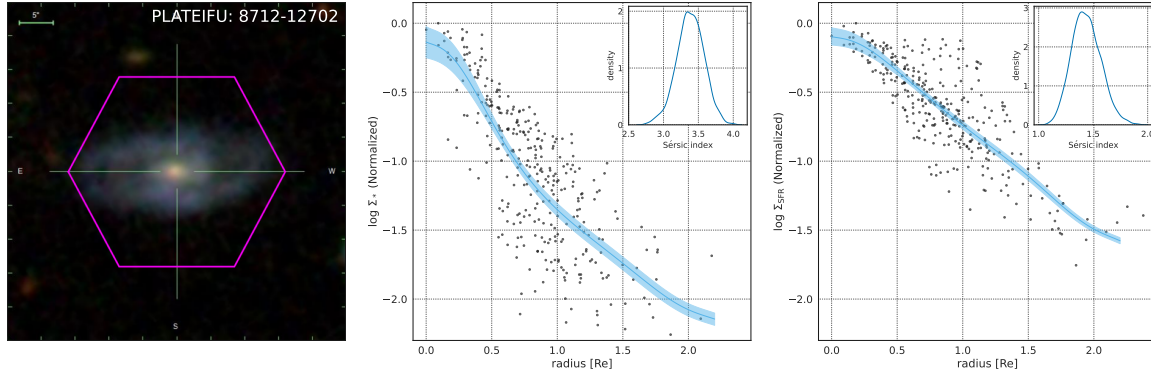


Figure 6. Examples of Sérsic profile fitting for stellar mass surface density (Σ_* , middle) and star formation rate surface density (Σ_{SFR} , right) maps of the same galaxy. The left panel shows the SDSS image of the galaxy. Black circles in the middle and right panels represent the observed radial profiles normalized by their maximum values. Cyan lines show the best-fitting PSF-convolved Sérsic models with shaded regions indicating the 95% confidence intervals. The insets show the probability density distributions of the Sérsic indices derived from the fitting.

deed harbor centrally concentrated star formation, and thus distinct populations from those with extended star formation over the galaxy disks.

We also note that for galaxies with central regions classified as AGN or composite, our Sérsic profile fitting uses only the available star-forming spaxels, creating gaps in their central Σ_{SFR} maps. These AGN host galaxies tend to have lower n_{SFR} values. This trend could result from potential star formation activity that may be present but obscured by AGN emission in the central regions, causing n_{SFR} to be underestimated in these galaxies. However, when we reproduce our main result’s figures using only non-AGN galaxies (Appendix A), the characteristic differences between the galaxy groups remain consistent.

3.2. Mean Specific SFR Radial Profiles

To investigate differences in the spatial distributions of star formation activity between MS-late and two MS-early subgroups, we compare their mean radial profiles of specific star formation rates (sSFR). For this purpose, we calculate weighted mean radial profiles for the $\text{H}\alpha$, $\text{H}\beta$, and stellar mass density maps using the elliptical coordinate maps provided in the MaNGA DAP for each galaxy. The coordinate is expressed in units of effective radius-normalized distance [R_e] (`bin_lwellcoo_r_re`). We calculate the weighted mean in bins of 0.5 R_e unit to obtain radial profiles for each galaxy (Figure 8). For the $\text{H}\alpha$ and $\text{H}\beta$ maps, we include all spaxels classified as star-forming or unclassified due to weak emission lines, while excluding those classified as composite or AGN. With this approach, we can properly include low S/N spaxels and avoid the bias toward the brightest star-forming regions.

Next, we compute the sSFR radial profiles from the weighted mean radial profiles of $\text{H}\alpha$, $\text{H}\beta$, and stellar

mass density, following the same procedure as described in Section 2.3. Before estimating the mean radial profiles, we normalize the sSFR radial profile of each galaxy by its mean sSFR value. This step is performed to remove the variations in the overall offset of individual galaxy profiles, allowing us to focus on the shape of the profiles. Here, we select normalization by the mean sSFR value rather than at a specific radius to minimize the impact of localized variations, thereby reducing scatter in the combined profiles.

We then divide both MS-late and MS-early into two stellar mass groups: low-mass ($8.5 \leq \log(M/M_\odot) < 9.75$) and high-mass ($9.75 \leq \log(M/M_\odot) < 11.0$), to account for potential stellar mass dependencies. Finally, we calculate the mean radial profiles for the 2×3 groups defined by stellar mass (low-mass or high-mass) and morphology (MS-late, MS-early_SF and MS-early_stellar).

Figure 9 presents the mean sSFR radial profiles. The error bars represent the 95% confidence intervals of the mean, assuming a t-distribution. Regardless of the stellar mass range, the MS-late galaxies show a profile with lower sSFR in their central regions and higher sSFR in their outer regions. This trend is consistent with previous studies focusing on MS galaxies (or late-type galaxies). Specifically, these galaxies have active star formation in their disk, while the central region have less active star formation compared to the disk, which is often cited as evidence for inside-out quenching. Interestingly, the MS-early_stellar galaxies display radial profiles remarkably similar to those of MS-late galaxies. This similarity suggests that MS-early_stellar galaxies might represent a more evolved state of MS-late galaxies, where the stellar bulge has grown more prominent while maintaining a similar pattern of star formation

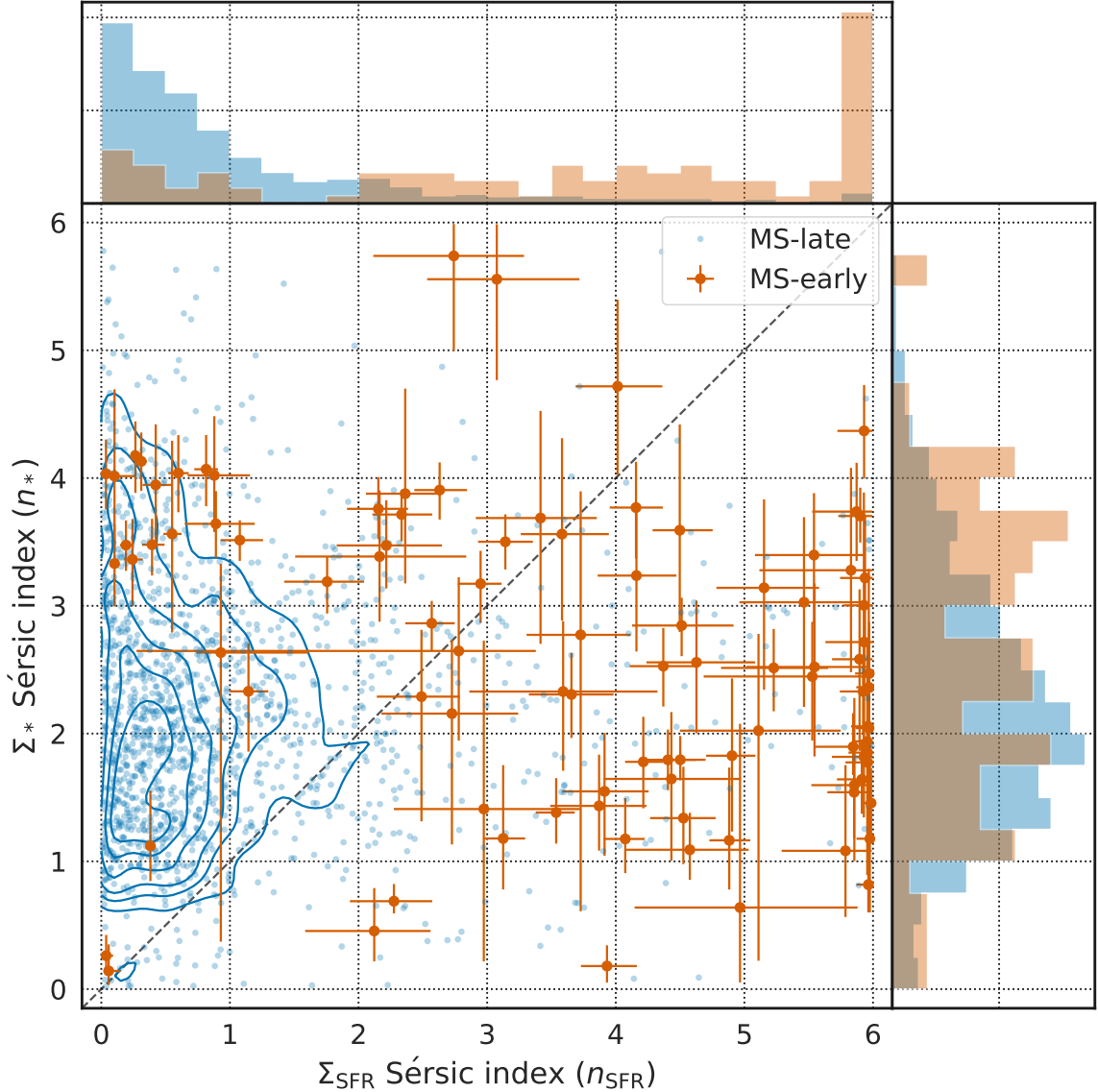


Figure 7. Distribution of Sérsic indices derived from Σ_{SFR} and Σ_* maps. In the main panel, the blue contours and circles represent the distribution of MS-late galaxies, while red circles show MS-early galaxies. Error bars on the MS-early points indicate the 95% confidence intervals from the Sérsic fitting. The dashed line represents where the Sérsic indices of Σ_{SFR} and Σ_* are equal. Top and right panels show the normalized histograms of the Sérsic indices for Σ_{SFR} and Σ_* , respectively, following the same color scheme as the main panel.

activity. In contrast, MS-early_SF galaxies show the opposite trend, with significantly enhanced sSFR in their center that rapidly decreases towards the outer region. This step gradient is consistent with their high n_{SFR} found in Section 3.1.

3.3. Resolved Main Sequence

Finally, we compare the relation between Σ_* and Σ_{SFR} , known as the resolved main sequence. The Σ_{SFR} values used in this analysis are dust-corrected as described in Section 2.3. Figure 10 presents the resolved main sequence for the MS-late, MS-early_SF, and MS-

early_stellar. To create the resolved main sequence, we plot each spaxel value on the Σ_* and Σ_{SFR} plane, and then calculate 2D histogram, which is represented by the black contour lines.

As shown in Figure 10, in the case of the MS-early_SF, the slope of the distribution appears steep. Orthogonal fitting reveals that the slope is 1.42 ± 0.03 , which is significantly steeper compared to the MS-late galaxies (0.771 ± 0.002). This suggests that, even compared to typical star-forming galaxies, the central star formation activity in the MS-early_SF is intense, indicating the presence of a central starburst. Conversely, the outer re-

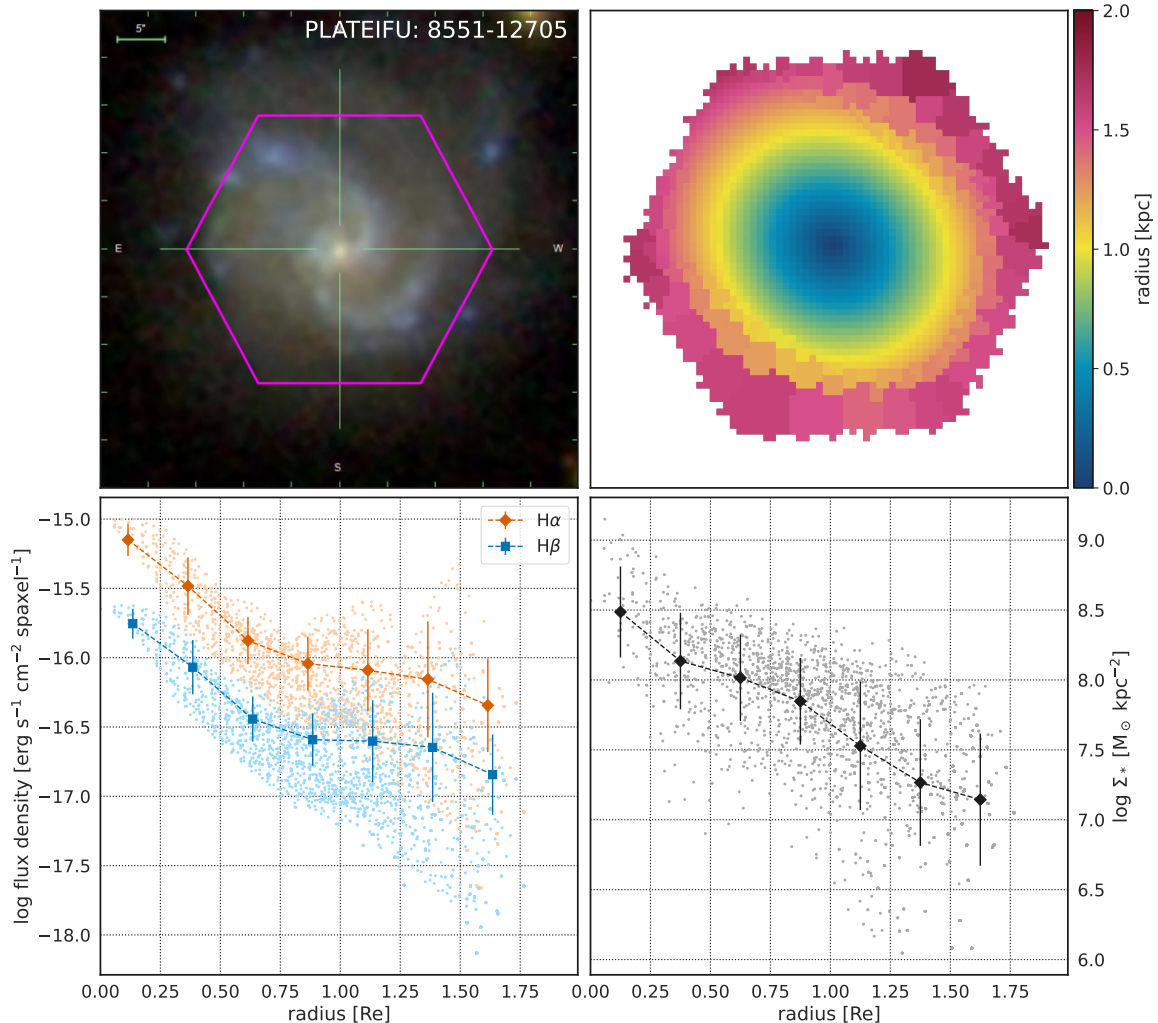


Figure 8. Example of the radial profile calculation process for a single galaxy. The top left panel shows the SDSS image of the galaxy, while the top right panel displays the corresponding MaNGA elliptical coordinate map. The bottom panels present the derived radial profiles: the $H\alpha$ and $H\beta$ profiles are shown in the bottom left (blue and red circles, respectively), and the stellar mass density profile is shown in the bottom right (black circles). In the radial profile panels, the diamonds with dashed lines and error bars indicate the weighted means and standard deviations in each radial bin.

regions exhibit less active star formation, leading to overall SFR that is comparable to the MS.

On the other hand, the slope of the distribution for the MS-early_stellar is 0.91 ± 0.02 , moderately steeper than that of the MS-late galaxies but much less than MS-early_SF. This steeper slope appears to be driven by moderately reduced Σ_{SFR} in outer regions rather than enhanced central star formation. These differences suggest that MS-early_stellar galaxies maintain star formation activity largely similar to MS-late galaxies, with only modest variations in their outer regions. As noted in Section 3.1, the Σ_* distribution in the MS-early_stellar is more centrally concentrated compared to both the MS-late and the MS-early_SF. This suggests that the MS-early_stellar galaxies are dominated by stellar bulges, similar to ellipticals, while maintain-

ing a spread-out distribution of star formation activity, that is a consistent result with the sSFR radial profiles in Section 3.2.

4. DISCUSSION

Our analysis revealed that MS-early galaxies can be further classified into two distinct subgroups: MS-early_SF and MS-early_stellar. These subgroups exhibit different star formation geometry despite both being located on the MS. To understand the origin of these subgroups, we further examine these populations in the perspectives of AGN activity and environmental effects.

4.1. AGN Activity

Active Galactic Nuclei (AGN) play a crucial role in galaxy evolution through their feedback effects on host

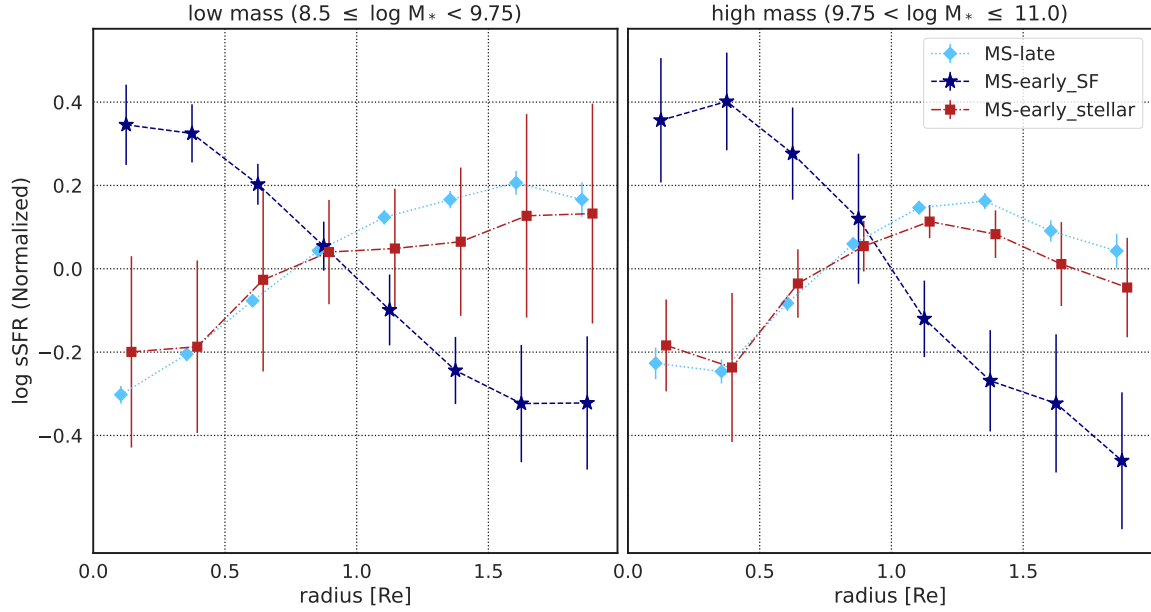


Figure 9. The mean sSFR radial profiles for the three galaxy groups: MS-late (light blue diamonds), MS-early_SF (navy stars), and MS-early_stellar (red squares). The error bars represent the 95% confidence intervals of the mean, assuming a t-distribution. The mean profiles are shown separately for low-mass ($8.5 \leq \log(M/M_\odot) < 9.75$; left panel) and high-mass ($9.75 \leq \log(M/M_\odot) < 11.0$; right panel) galaxies.

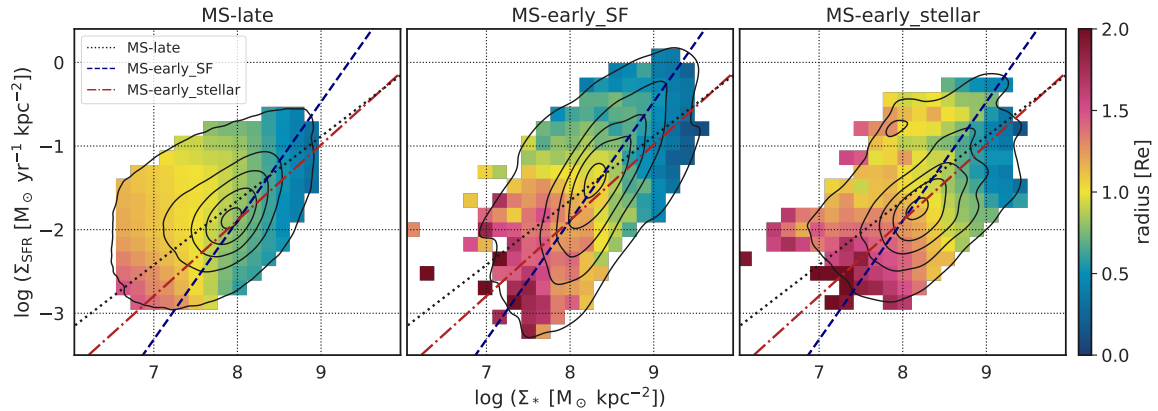


Figure 10. The resolved main sequence (the relation between $\log \Sigma_*$ and $\log \Sigma_{\text{SFR}}$) for the three galaxy groups. From left to right, the panels show the distributions for MS-late, MS-early_SF, and MS-early_stellar galaxies. In each panel, the contours represent the 2D histogram of spaxel values, and the overlaid colormaps show the mean radius [R_e] calculated for each bin in the $\log \Sigma_*$ - $\log \Sigma_{\text{SFR}}$ space with bin sizes of ~ 0.17 dex. The three lines indicate the results of orthogonal fitting to the distributions. The black dotted line corresponds to the MS-late, the blue dashed line corresponds to the MS-early_SF, and the red dot-dashed line corresponds to the MS-early_stellar.

galaxies (Fabian 2012; Harrison 2017). Since strong AGN emission can affect both galaxy properties and their morphological classification, it is important to examine the relationship between the presence of AGN and our galaxy subgroups.

We identify AGN hosts by requiring multiple spaxels within $0.5 R_e$ to be classified as AGN through BPT diagnostics. This requirement helps minimize false positives that could arise from measurement uncertainties in

single spaxels. The Figure 11 shows that approximately half of the MS-early_stellar galaxies host AGN, while AGN are rare in the MS-early_SF galaxies. However, this distinction appears to be primarily a consequence of the different stellar mass distributions between these subgroups rather than an intrinsic characteristic of the classifications themselves. As shown by the gray circles, the AGN fraction exhibits a strong mass dependence, with higher-mass galaxies more likely to host AGN. The

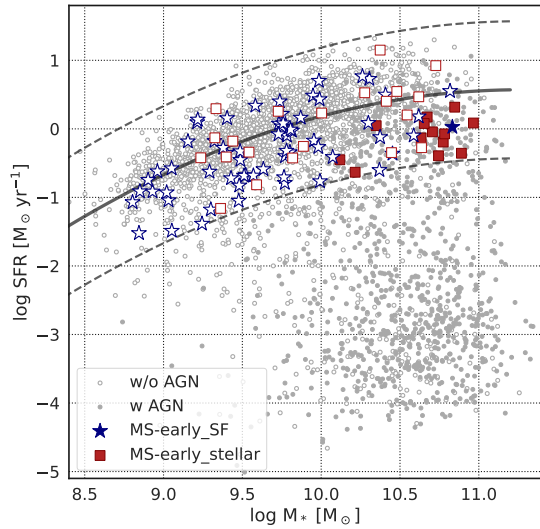


Figure 11. The relation between stellar mass (M_*) and star formation rate (SFR). Gray circles show the full sample, while blue stars and red squares represent the MS-early_SF and the MS-early_stellar galaxies, respectively. Filled symbols indicate AGN host galaxies, while open symbols represent non-AGN galaxies.

stellar mass distribution of MS-early_stellar galaxies is biased toward higher masses ($\log M_*/M_\odot > 10$), while MS-early_SF galaxies tend to have a lower mass. This systematic difference in stellar mass distribution naturally accounts for the observed difference in AGN fractions between the two subgroups.

It is also important to note that our analysis excludes spaxels classified as AGN or composite to measure pure star formation activity. While this approach is necessary to avoid AGN contamination, it may lead to an underestimation of Σ_{SFR} (and SFR) in AGN host galaxies, particularly in their central regions. This can also affect the accuracy of our radial profile measurements. To assess the impact of this limitation, we have performed the same analyses (sSFR radial profiles and the resolved MS) using only non-AGN galaxies, as presented in Appendix A (Figure A1 and A2). We confirm that the results are basically identical to those presented in Figure 9 and 10, demonstrating that our main conclusions are unaffected by the AGN effects.

4.2. Environmental Effects

Galaxy environment affects galaxy evolution through various physical mechanisms. High-density environments facilitate galaxy interactions and mergers that can trigger morphological transformation and enhanced star formation. In cluster environments, additional processes such as ram pressure stripping and galaxy harassment

can dramatically influence galaxy properties (Boselli & Gavazzi 2006).

We first examine the halo mass (M_h) estimates from the SDSS galaxy group catalog (Tinker 2020, 2021). This catalog identifies galaxy groups using a friends-of-friends algorithm and assigns halo masses based on the total stellar mass of the group members. The left panel of Figure 12 shows the M_*-M_h relation for our galaxy subgroups. The gray circles representing the full sample demonstrate a strong correlation between stellar and halo mass, consistent with previous studies (e.g., Moster et al. 2010; Behroozi et al. 2013). This correlation is primarily defined by the MS galaxies, which dominate our sample. The broken line traces the peak values of the 2D kernel density estimation at each stellar mass, representing the typical M_*-M_h relation. This line also clearly shows the underlying mass-density relation, where more massive galaxies reside in higher mass halos (i.e., denser environments). We find that the MS-early_stellar galaxies follow this same correlation, suggesting that they inhabit environments similar to those of typical MS galaxies.

In contrast, the MS-early_SF galaxies systematically deviate from the M_*-M_h relation toward higher M_h at fixed M_* . This deviation indicates that MS-early_SF galaxies represent outliers from the typical stellar mass-environment relation, residing in environments that are denser than expected for their stellar masses. The right panel of Figure 12 shows the cumulative distribution functions of halo mass offsets ($\log M_h/M_h^*$) from the predicted M_*-M_h relation, where M_h^* is the predicted halo mass based on each galaxy’s stellar mass. The cumulative distributions clearly show that MS-early_SF galaxies exhibit much larger systematic deviations from MS-late galaxies compared to MS-early_stellar galaxies, with MS-early_SF galaxies showing systematic positive offsets with a median of approximately 0.6 dex. Kolmogorov-Smirnov tests comparing each MS-early subgroup with MS-late galaxies yield p-values of 2.4×10^{-19} for MS-early_SF and 0.027 for MS-early_stellar. This also confirms that MS-early_SF galaxies show much larger deviations than MS-early_stellar galaxies. This systematic offset toward higher M_h implies that MS-early_SF galaxies reside in denser environments than typical MS galaxies, even after accounting for the general mass-environment correlation.

To further confirm this environmental difference, we also compare the local density distribution using the normalized local density parameter η_k from the GEMAVAC (Argudo-Fernández et al. 2015). This parameter is defined as the number density within the projected distance to the 5th nearest neighbor, with higher val-

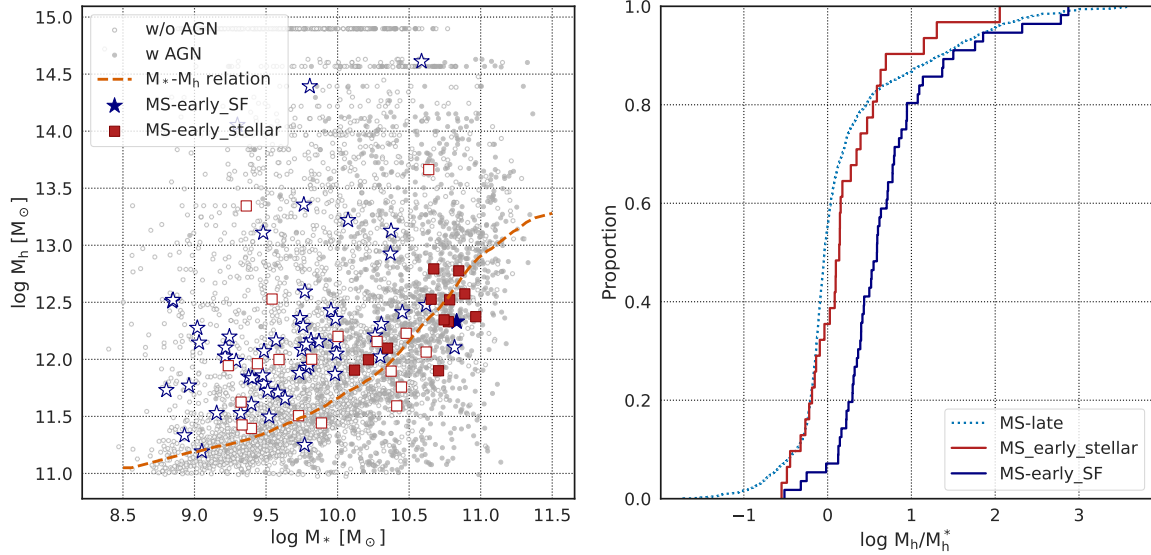


Figure 12. Left: The relation between stellar mass and halo mass. Gray circles show the full sample, while blue stars and red squares represent the MS-early_SF and the MS-early_stellar galaxies, respectively. Filled symbols indicate AGN host galaxies, while open symbols represent non-AGN galaxies. The broken line shows the M_* - M_h relation defined by the overall sample. Right: Cumulative distribution of the offset in M_h from the M_* - M_h relation ($\log M_h/M_h^*$, where M_h^* is the predicted M_h from their M_*) for the MS-late, MS-early_stellar, and MS-early_SF galaxies.

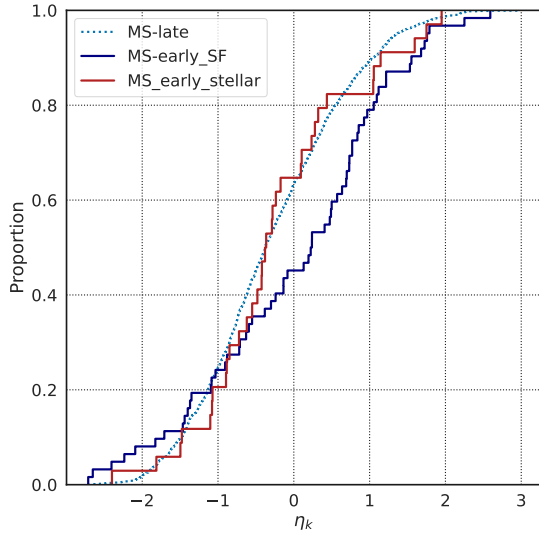


Figure 13. Cumulative distribution of local density (η_k) for the three groups. The light blue dotted line represents the MS-late galaxies, while the blue and red solid lines show the MS-early_SF and the MS-early_stellar galaxies, respectively.

ues of η_k indicating higher local densities. Figure 13 shows the η_k distributions for each subgroup. The MS-early_stellar galaxies exhibit a η_k distribution similar to those of MS-late galaxies, while the MS-early_SF galaxies show significantly higher local densities, with a median η_k value 0.6 dex higher than that of MS-late galaxies. We perform Kolmogorov-Smirnov tests to compare the distributions of MS-early subgroups with that of

MS-late galaxies. The resulting p-values are 0.905 for MS-early_stellar and 0.002 for MS-early_SF. At a significance level of 1 %, the MS-early_SF distribution differs significantly from that of MS-late galaxies.

4.3. Formation Pathways of MS-early Galaxies

Our analysis reveals that early-type galaxies on the MS consist of two distinct populations with different Σ_{SFR} , Σ_* geometries and environments, suggesting different formation pathways for each population.

The MS-early_stellar galaxies maintain disk-like star formation patterns similar to MS-late galaxies while exhibiting more concentrated stellar mass distributions (Section 3.2). Their environmental properties are also remarkably similar to those of MS-late galaxies, showing no evidence for environmental effects (Section 4.2). These observational features suggest that MS-early_stellar galaxies evolve primarily through internal secular processes (Kormendy & Kennicutt 2004; Sachdeva et al. 2017). They appear to be simply the most bulge-dominated subset of the star-forming galaxy population, where secular evolution has gradually built up their central stellar mass while maintaining their disk-like star formation patterns. MS-early_stellar and MS-late galaxies thus likely represent different stages along a common evolutionary sequence characterized by their degree of central mass concentration.

In contrast, MS-early_SF galaxies show clear evidence of environmentally-driven evolution. These galaxies have centrally concentrated star formation (Section 3.2)

and are found in moderately denser environments than typical MS galaxies (Section 4.2). Our analysis reveals that MS-early_SF galaxies typically reside in environments with 0.6 dex higher local densities (η_k) compared to MS-late or MS-early_stellar galaxies. This density enhancement corresponds to pair or group-scale environments rather than massive clusters or isolated field regions.

Considering the fact that MS-early_SF galaxies are also a subsample of the MS galaxies, it is expected that they are not strong starbursts. Nevertheless, our result demonstrates that such galaxies characterized by the unique internal SF geometry are preferentially triggered by group-scale environment, suggesting that those intermediate-density environments are capable of driving the gas toward galaxy centers, triggering localized starburst-like activity without disrupting the entire galaxy. Previous studies have shown similar effects where interactions can redistribute gas within galaxies (e.g., Moreno et al. 2015; Blumenthal & Barnes 2018). The concentrated star formation in these galaxies suggests an ongoing buildup of central stellar mass, which may eventually lead to more prominent bulge-like structures. This process appears to represent an early phase of environmentally-influenced morphological evolution that connects with the well-known trend of increasing bulge fraction in group and cluster environments (e.g., Dressler 1980). Additionally, the centrally concentrated star formation activity observed in MS-early_SF galaxies may be relevant to the formation of positive age gradients found in some early-type galaxies (e.g., Rawle et al. 2010; Koleva et al. 2011; San Roman et al. 2018; Parikh et al. 2021), where central regions contain relatively younger stellar populations than the outer regions. While we cannot directly trace the full evolutionary sequence with our data, the MS-early_SF galaxies provide an important snapshot of environmental processes shaping galaxy structure before a stellar bulge is fully established.

In this study, we have revealed distinct subgroups *amongst* MS galaxies that share similar global properties but follow different evolutionary pathways, by incorporating spatially-resolved properties. We emphasize the importance to combine the global measurements and the internal structure analysis to understand the true diversity of star-forming galaxies. While global measurements of galaxy properties characterized by e.g. the location on the MS diagram or the visual morphology are of course helpful to describe the nature of galaxies in a statistical way, the spatially integrated measurements alone cannot fully capture the diversity within the MS population.

5. SUMMARY

We investigated the diversity within the MS galaxy population by using spatially-resolved data from the MaNGA final data release. Following the morphological classifications from the MaNGA Morphology Deep Learning catalog, we identified a sample of 1587 “MS-late” and 97 “MS-early” galaxies that show similar global star formation properties but different morphologies. Our main findings are as follows:

1. Through Sérsic profile fitting of Σ_{SFR} and Σ_* maps, we found that the MS-early galaxies can be further classified into two subgroups based on their structural properties—i.e. “MS-early_SF” (63 galaxies) and “MS-early_stellar” (34 galaxies). The “MS-early_SF” galaxies show higher Sérsic indices in Σ_{SFR} than Σ_* , indicating centrally concentrated star formation, while the MS-early_stellar galaxies exhibit lower Sérsic indices in Σ_{SFR} than Σ_* , suggesting extended star formation similar to the MS-late galaxies.
2. We found a clear difference in the mean sSFR radial profile between the two subgroups. The MS-early_SF galaxies show significantly enhanced central star formation with rapidly declining sSFR toward the outer regions. In contrast, the MS-early_stellar galaxies exhibit profiles similar to the MS-late galaxies, characterized by suppressed central star formation and relatively flat sSFR distributions in their outer regions.
3. We studied the resolved SFR– M_* relation, and found that the MS-early_SF galaxies show steeper slopes in their Σ_* – Σ_{SFR} relations compared to the MS-late or MS-early_stellar galaxies, demonstrating their intense central star formation activity. On the other hand, the slope of the resolved main sequence for the MS-early_stellar galaxies is similar to that of the MS-late galaxies, although the MS-early_stellar galaxies show more concentrated stellar mass distribution than MS-late galaxies.
4. Approximately half of the MS-early_stellar galaxies host AGNs, while AGNs are rare in the MS-early_SF galaxies. We note that this difference would reflect their different stellar mass distributions (the MS-early_stellar galaxies tend to be more massive than MS-early_SF). However, our conclusions are unchanged even if we use only non-AGN galaxies.
5. The MS-early_SF galaxies tend to reside in different environment than MS-early_stellar or MS-

late galaxies. The MS-early_stellar galaxies have similar halo masses and local densities to those of the MS-late galaxies. In contrast, the MS-early_SF galaxies show systematic environmental differences. They typically have 0.6 dex higher halo masses at fixed stellar mass (based on median values) and reside in environments with 0.6 dex higher local densities compared to MS-late galaxies. These significant environmental differences suggest distinct formation mechanisms between these populations.

6. Our results imply that there exist two different evolutionary pathways among the MS galaxies with early-type morphologies. The MS-early_stellar galaxies share similar environments to MS-late galaxies and maintain disk-like star formation patterns, suggesting they evolve through internal processes that gradually build up central mass. The MS-early_SF galaxies, in contrast, reside in denser group-scale environments and show centrally concentrated star formation. This environmental connection suggests that interactions in these denser regions drive gas toward galaxy centers, triggering intense localized star formation. While these galaxies lack stellar bulges, their concentrated star formation activity may represent an early phase of environmentally-driven morphological evolution, potentially connecting to the higher bulge fractions observed in group and cluster environments.

We emphasize again that, while the positions on the SFR- M_* diagram can provide a basic information to characterize the nature of galaxies, there exist diverse galaxy populations even at a fixed stellar mass and SFR. By combining the global and spatially-resolved properties of galaxies, we now identified distinct subgroups among the MS galaxies—galaxies sharing similar global star formation properties but likely followed via different evolutionary pathways. Our results demonstrate that spatially-resolved information from IFS observations is critical for understanding the full picture of galaxy evolution.

We thank the anonymous referee for careful reading and useful comments that helped to improve our paper. Funding for the Sloan Digital Sky Survey IV has been provided by the Alfred P. Sloan Foundation, the U.S. Department of Energy Office of Science, and the Participating Institutions. SDSS-IV acknowledges support and resources from the Center for High Performance Computing at the University of Utah. The SDSS website is www.sdss4.org. SDSS-IV is managed by the Astrophysical Research Consortium for the Participating Institutions of the SDSS Collaboration including the Brazilian Participation Group, the Carnegie Institution for Science, Carnegie Mellon University, Center for Astrophysics — Harvard & Smithsonian, the Chilean Participation Group, the French Participation Group, Instituto de Astrofísica de Canarias, The Johns Hopkins University, Kavli Institute for the Physics and Mathematics of the Universe (IPMU) / University of Tokyo, the Korean Participation Group, Lawrence Berkeley National Laboratory, Leibniz Institut für Astrophysik Potsdam (AIP), Max-Planck-Institut für Astronomie (MPIA Heidelberg), Max-Planck-Institut für Astrophysik (MPA Garching), Max-Planck-Institut für Extraterrestrische Physik (MPE), National Astronomical Observatories of China, New Mexico State University, New York University, University of Notre Dame, Observatório Nacional / MCTI, The Ohio State University, Pennsylvania State University, Shanghai Astronomical Observatory, United Kingdom Participation Group, Universidad Nacional Autónoma de México, University of Arizona, University of Colorado Boulder, University of Oxford, University of Portsmouth, University of Utah, University of Virginia, University of Washington, University of Wisconsin, Vanderbilt University, and Yale University. YK acknowledge support from JSPS KAKENHI grant No.23H01219 and JSPS Core-to-Core Program (grant No.JPJSCCA20210003).

Software: Astropy (Astropy Collaboration et al. 2013, 2018, 2022), NumPy (Harris et al. 2020), SciPy (Virtanen et al. 2020), Pandas (pandas development team 2020), Matplotlib (Hunter 2007), JAX (Bradbury et al. 2018), NumPyro (Phan et al. 2019; Bingham et al. 2019), Marvin (Cherinka et al. 2019),

REFERENCES

- Abdurro’uf, Accetta, K., Aerts, C., et al. 2022, *ApJS*, 259, 35, doi: [10.3847/1538-4365/ac4414](https://doi.org/10.3847/1538-4365/ac4414)
- Aguado, D. S., Ahumada, R., Almeida, A., et al. 2019, *ApJS*, 240, 23, doi: [10.3847/1538-4365/aaf651](https://doi.org/10.3847/1538-4365/aaf651)
- Argudo-Fernández, M., Verley, S., Bergond, G., et al. 2015, *A&A*, 578, A110, doi: [10.1051/0004-6361/201526016](https://doi.org/10.1051/0004-6361/201526016)

- Astropy Collaboration, Robitaille, T. P., Tollerud, E. J., et al. 2013, *A&A*, 558, A33, doi: [10.1051/0004-6361/201322068](https://doi.org/10.1051/0004-6361/201322068)
- Astropy Collaboration, Price-Whelan, A. M., Sipőcz, B. M., et al. 2018, *AJ*, 156, 123, doi: [10.3847/1538-3881/aabc4f](https://doi.org/10.3847/1538-3881/aabc4f)
- Astropy Collaboration, Price-Whelan, A. M., Lim, P. L., et al. 2022, *ApJ*, 935, 167, doi: [10.3847/1538-4357/ac7c74](https://doi.org/10.3847/1538-4357/ac7c74)
- Baldwin, J. A., Phillips, M. M., & Terlevich, R. 1981, *PASP*, 93, 5, doi: [10.1086/130766](https://doi.org/10.1086/130766)
- Behroozi, P. S., Wechsler, R. H., & Conroy, C. 2013, *ApJ*, 770, 57, doi: [10.1088/0004-637X/770/1/57](https://doi.org/10.1088/0004-637X/770/1/57)
- Belfiore, F., Maiolino, R., Bundy, K., et al. 2018, *MNRAS*, 477, 3014, doi: [10.1093/mnras/sty768](https://doi.org/10.1093/mnras/sty768)
- Bell, E. F., van der Wel, A., Papovich, C., et al. 2012, *ApJ*, 753, 167, doi: [10.1088/0004-637X/753/2/167](https://doi.org/10.1088/0004-637X/753/2/167)
- Bingham, E., Chen, J. P., Jankowiak, M., et al. 2019, *J. Mach. Learn. Res.*, 20, 28:1. <http://jmlr.org/papers/v20/18-403.html>
- Blanton, M. R., Bershad, M. A., Abolfathi, B., et al. 2017, *AJ*, 154, 28, doi: [10.3847/1538-3881/aa7567](https://doi.org/10.3847/1538-3881/aa7567)
- Blumenthal, K. A., & Barnes, J. E. 2018, *MNRAS*, 479, 3952, doi: [10.1093/mnras/sty1605](https://doi.org/10.1093/mnras/sty1605)
- Boselli, A., & Gavazzi, G. 2006, *PASP*, 118, 517, doi: [10.1086/500691](https://doi.org/10.1086/500691)
- Bradbury, J., Frostig, R., Hawkins, P., et al. 2018, JAX: composable transformations of Python+NumPy programs, 0.3.13. <http://github.com/jax-ml/jax>
- Bundy, K., Bershad, M. A., Law, D. R., et al. 2015, *ApJ*, 798, 7, doi: [10.1088/0004-637X/798/1/7](https://doi.org/10.1088/0004-637X/798/1/7)
- Cappellari, M., & Copin, Y. 2003, *MNRAS*, 342, 345, doi: [10.1046/j.1365-8711.2003.06541.x](https://doi.org/10.1046/j.1365-8711.2003.06541.x)
- Cardelli, J. A., Clayton, G. C., & Mathis, J. S. 1989, *ApJ*, 345, 245, doi: [10.1086/167900](https://doi.org/10.1086/167900)
- Cherinka, B., Andrews, B. H., Sánchez-Gallego, J., et al. 2019, *AJ*, 158, 74, doi: [10.3847/1538-3881/ab2634](https://doi.org/10.3847/1538-3881/ab2634)
- Croom, S. M., Lawrence, J. S., Bland-Hawthorn, J., et al. 2012, *MNRAS*, 421, 872, doi: [10.1111/j.1365-2966.2011.20365.x](https://doi.org/10.1111/j.1365-2966.2011.20365.x)
- Daddi, E., Dickinson, M., Morrison, G., et al. 2007, *ApJ*, 670, 156, doi: [10.1086/521818](https://doi.org/10.1086/521818)
- Domínguez Sánchez, H., Margalef, B., Bernardi, M., & Huertas-Company, M. 2022, *MNRAS*, 509, 4024, doi: [10.1093/mnras/stab3089](https://doi.org/10.1093/mnras/stab3089)
- Dressler, A. 1980, *ApJ*, 236, 351, doi: [10.1086/157753](https://doi.org/10.1086/157753)
- Elbaz, D., Daddi, E., Le Borgne, D., et al. 2007, *A&A*, 468, 33, doi: [10.1051/0004-6361:20077525](https://doi.org/10.1051/0004-6361:20077525)
- Ellison, S. L., Sánchez, S. F., Ibarra-Medel, H., et al. 2018, *MNRAS*, 474, 2039, doi: [10.1093/mnras/stx2882](https://doi.org/10.1093/mnras/stx2882)
- Fabian, A. C. 2012, *ARA&A*, 50, 455, doi: [10.1146/annurev-astro-081811-125521](https://doi.org/10.1146/annurev-astro-081811-125521)
- Foster, L. M., Parker, L. C., Gwyn, S., et al. 2025, *ApJ*, 982, 120, doi: [10.3847/1538-4357/adb8dc](https://doi.org/10.3847/1538-4357/adb8dc)
- Goddard, D., Thomas, D., Maraston, C., et al. 2017, *MNRAS*, 466, 4731, doi: [10.1093/mnras/stw3371](https://doi.org/10.1093/mnras/stw3371)
- Gunn, J. E., Siegmund, W. A., Mannery, E. J., et al. 2006, *AJ*, 131, 2332, doi: [10.1086/500975](https://doi.org/10.1086/500975)
- Harris, C. R., Millman, K. J., van der Walt, S. J., et al. 2020, *Nature*, 585, 357–362, doi: [10.1038/s41586-020-2649-2](https://doi.org/10.1038/s41586-020-2649-2)
- Harrison, C. M. 2017, *Nature Astronomy*, 1, 0165, doi: [10.1038/s41550-017-0165](https://doi.org/10.1038/s41550-017-0165)
- Hunter, J. D. 2007, *Computing in Science & Engineering*, 9, 90, doi: [10.1109/MCSE.2007.55](https://doi.org/10.1109/MCSE.2007.55)
- Kauffmann, G., Heckman, T. M., Tremonti, C., et al. 2003, *MNRAS*, 346, 1055, doi: [10.1111/j.1365-2966.2003.07154.x](https://doi.org/10.1111/j.1365-2966.2003.07154.x)
- Kennicutt, Robert C., J., Tamblyn, P., & Congdon, C. E. 1994, *ApJ*, 435, 22, doi: [10.1086/174790](https://doi.org/10.1086/174790)
- Kennicutt, R. C., & Evans, N. J. 2012, *ARA&A*, 50, 531, doi: [10.1146/annurev-astro-081811-125610](https://doi.org/10.1146/annurev-astro-081811-125610)
- Kewley, L. J., Groves, B., Kauffmann, G., & Heckman, T. 2006, *MNRAS*, 372, 961, doi: [10.1111/j.1365-2966.2006.10859.x](https://doi.org/10.1111/j.1365-2966.2006.10859.x)
- Koleva, M., Prugniel, P., De Rijcke, S., & Zeilinger, W. W. 2011, *MNRAS*, 417, 1643, doi: [10.1111/j.1365-2966.2011.19057.x](https://doi.org/10.1111/j.1365-2966.2011.19057.x)
- Kormendy, J., & Kennicutt, Robert C., J. 2004, *ARA&A*, 42, 603, doi: [10.1146/annurev.astro.42.053102.134024](https://doi.org/10.1146/annurev.astro.42.053102.134024)
- Koyama, Y., Smail, I., Kurk, J., et al. 2013, *MNRAS*, 434, 423, doi: [10.1093/mnras/stt1035](https://doi.org/10.1093/mnras/stt1035)
- Kroupa, P. 2001, *MNRAS*, 322, 231, doi: [10.1046/j.1365-8711.2001.04022.x](https://doi.org/10.1046/j.1365-8711.2001.04022.x)
- Law, D. R., Cherinka, B., Yan, R., et al. 2016, *AJ*, 152, 83, doi: [10.3847/0004-6256/152/4/83](https://doi.org/10.3847/0004-6256/152/4/83)
- Lintott, C., Schawinski, K., Bamford, S., et al. 2011, *MNRAS*, 410, 166, doi: [10.1111/j.1365-2966.2010.17432.x](https://doi.org/10.1111/j.1365-2966.2010.17432.x)
- Maraston, C., Hill, L., Thomas, D., et al. 2020, *MNRAS*, 496, 2962, doi: [10.1093/mnras/staa1489](https://doi.org/10.1093/mnras/staa1489)
- Masters, K. L., Krawczyk, C., Shamsi, S., et al. 2021, *MNRAS*, 507, 3923, doi: [10.1093/mnras/stab2282](https://doi.org/10.1093/mnras/stab2282)
- Medling, A. M., Cortese, L., Croom, S. M., et al. 2018, *MNRAS*, 475, 5194, doi: [10.1093/mnras/sty127](https://doi.org/10.1093/mnras/sty127)
- Moreno, J., Torrey, P., Ellison, S. L., et al. 2015, *MNRAS*, 448, 1107, doi: [10.1093/mnras/stv094](https://doi.org/10.1093/mnras/stv094)
- Moster, B. P., Somerville, R. S., Maulbetsch, C., et al. 2010, *ApJ*, 710, 903, doi: [10.1088/0004-637X/710/2/903](https://doi.org/10.1088/0004-637X/710/2/903)
- Nair, P. B., & Abraham, R. G. 2010, *ApJS*, 186, 427, doi: [10.1088/0067-0049/186/2/427](https://doi.org/10.1088/0067-0049/186/2/427)
- Neumann, J., Thomas, D., Maraston, C., et al. 2022, *MNRAS*, 513, 5988, doi: [10.1093/mnras/stac1260](https://doi.org/10.1093/mnras/stac1260)

- pandas development team, T. 2020, pandas-dev/pandas: Pandas, latest, Zenodo, doi: [10.5281/zenodo.3509134](https://doi.org/10.5281/zenodo.3509134)
- Parikh, T., Thomas, D., Maraston, C., et al. 2021, MNRAS, 502, 5508, doi: [10.1093/mnras/stab449](https://doi.org/10.1093/mnras/stab449)
- Peng, Y.-j., Lilly, S. J., Kovač, K., et al. 2010, ApJ, 721, 193, doi: [10.1088/0004-637X/721/1/193](https://doi.org/10.1088/0004-637X/721/1/193)
- Phan, D., Pradhan, N., & Jankowiak, M. 2019, arXiv preprint arXiv:1912.11554
- Planck Collaboration, Aghanim, N., Akrami, Y., et al. 2020, A&A, 641, A6, doi: [10.1051/0004-6361/201833910](https://doi.org/10.1051/0004-6361/201833910)
- Rawle, T. D., Smith, R. J., & Lucey, J. R. 2010, MNRAS, 401, 852, doi: [10.1111/j.1365-2966.2009.15722.x](https://doi.org/10.1111/j.1365-2966.2009.15722.x)
- Ren, J., Liu, F. S., Li, N., et al. 2024, ApJ, 969, 4, doi: [10.3847/1538-4357/ad4117](https://doi.org/10.3847/1538-4357/ad4117)
- Sachdeva, S., Saha, K., & Singh, H. P. 2017, ApJ, 840, 79, doi: [10.3847/1538-4357/aa6c61](https://doi.org/10.3847/1538-4357/aa6c61)
- Salim, S., Boquien, M., & Lee, J. C. 2018, ApJ, 859, 11, doi: [10.3847/1538-4357/aabf3c](https://doi.org/10.3847/1538-4357/aabf3c)
- Salim, S., Lee, J. C., Janowiecki, S., et al. 2016, ApJS, 227, 2, doi: [10.3847/0067-0049/227/1/2](https://doi.org/10.3847/0067-0049/227/1/2)
- Salvador, D., Cerulo, P., Valenzuela, K., et al. 2024, A&A, 684, A166, doi: [10.1051/0004-6361/202347522](https://doi.org/10.1051/0004-6361/202347522)
- San Roman, I., Cenarro, A. J., Díaz-García, L. A., et al. 2018, A&A, 609, A20, doi: [10.1051/0004-6361/201630313](https://doi.org/10.1051/0004-6361/201630313)
- Sánchez-Blázquez, P., Peletier, R. F., Jiménez-Vicente, J., et al. 2006, MNRAS, 371, 703, doi: [10.1111/j.1365-2966.2006.10699.x](https://doi.org/10.1111/j.1365-2966.2006.10699.x)
- Tinker, J. L. 2020, arXiv e-prints, arXiv:2007.12200, doi: [10.48550/arXiv.2007.12200](https://doi.org/10.48550/arXiv.2007.12200)
- . 2021, ApJ, 923, 154, doi: [10.3847/1538-4357/ac2aaa](https://doi.org/10.3847/1538-4357/ac2aaa)
- van der Wel, A., Franx, M., van Dokkum, P. G., et al. 2014, ApJ, 788, 28, doi: [10.1088/0004-637X/788/1/28](https://doi.org/10.1088/0004-637X/788/1/28)
- Virtanen, P., Gommers, R., Oliphant, T. E., et al. 2020, Nature Methods, 17, 261, doi: [10.1038/s41592-019-0686-2](https://doi.org/10.1038/s41592-019-0686-2)
- Westfall, K. B., Cappellari, M., Bershady, M. A., et al. 2019, AJ, 158, 231, doi: [10.3847/1538-3881/ab44a2](https://doi.org/10.3847/1538-3881/ab44a2)
- Wilkinson, D. M., Maraston, C., Goddard, D., Thomas, D., & Parikh, T. 2017, MNRAS, 472, 4297, doi: [10.1093/mnras/stx2215](https://doi.org/10.1093/mnras/stx2215)
- Willett, K. W., Lintott, C. J., Bamford, S. P., et al. 2013, MNRAS, 435, 2835, doi: [10.1093/mnras/stt1458](https://doi.org/10.1093/mnras/stt1458)
- Wuyts, S., Förster Schreiber, N. M., van der Wel, A., et al. 2011, ApJ, 742, 96, doi: [10.1088/0004-637X/742/2/96](https://doi.org/10.1088/0004-637X/742/2/96)

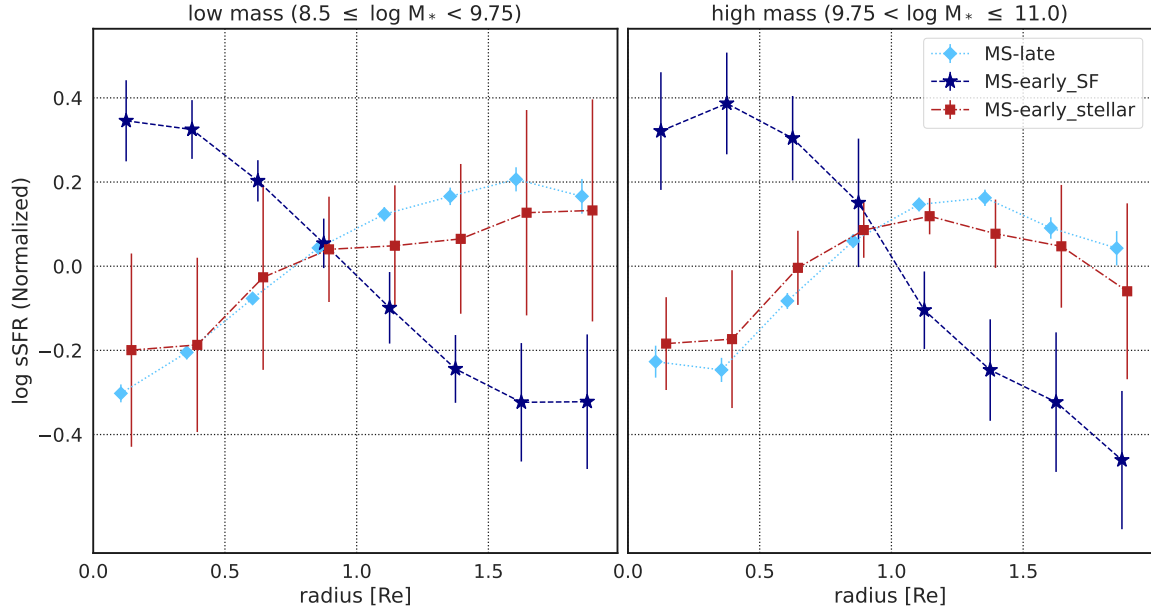


Figure A1. The mean sSFR radial profiles for non-AGN galaxies in the three groups: MS-late (light blue diamonds), MS-early_SF (navy stars), and MS-early_stellar (red squares). As in Figure 9, the error bars represent the 95% confidence intervals of the mean, assuming a t-distribution, and profiles are shown separately for low-mass ($8.5 \leq \log(M/M_{\odot}) < 9.75$; left panel) and high-mass ($9.75 \leq \log(M/M_{\odot}) < 11.0$; right panel) galaxies.

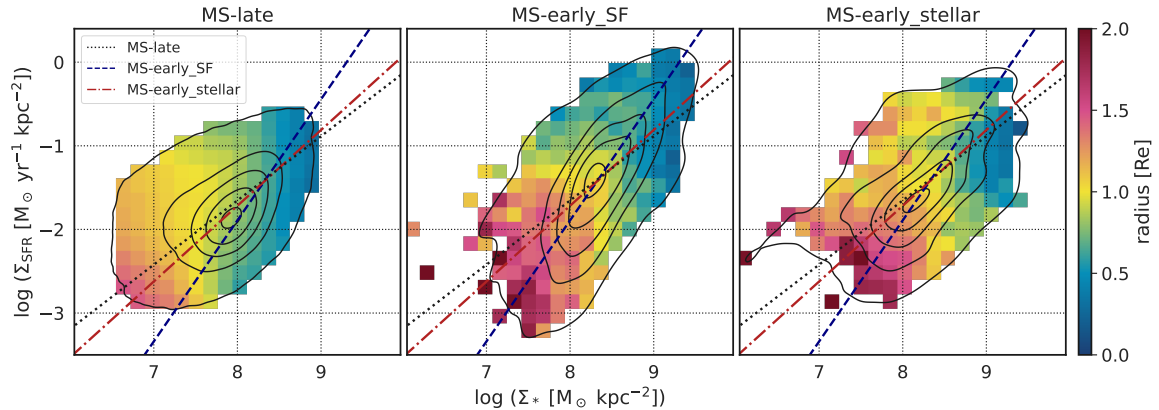


Figure A2. The resolved main sequence for non-AGN galaxies in the three groups. From left to right, the panels show the distributions for MS-late, MS-early_SF, and MS-early_stellar galaxies. As in Figure 10, contours represent the 2D histogram of spaxel values, and the overlaid colormaps correspond to the mean radius $[R_e]$ at each position. The three lines indicate the results of orthogonal fitting to the distributions. The black dotted line corresponds to the MS-late, the blue dashed line corresponds to the MS-early_SF, and the red dot-dashed line corresponds to the MS-early_stellar.

APPENDIX

A. ANALYSIS EXCLUDING AGN HOST GALAXIES

To verify that our results are not significantly affected by AGN in our analysis, we reproduce our main result's figures using only non-AGN galaxies. Figure A1 shows the mean sSFR radial profiles, and Figure A2 presents the resolved main sequence relations for galaxies without AGN. The patterns observed in these figures are nearly identical to those presented in Figures 9 and 10, respectively, confirming that our main conclusions are robust against potential AGN effects.